

Experimental and Monte Carlo Simulation Studies to Investigate the Working Principle of Compact Nanodosimeters*

Victor Merza^{a,b,c,*}, Aleksandr Bancer^{d,e}, Vladimir Bashkirov^c, Ana Belchior^{a,b}, Beata Brzozowska^f, João F. Canhoto^{a,b}, Piotr Gasik^{g,h}, Jaroslaw Grzyb^e, Khaled Katmeh^{a,b}, Marcin Pietrzak^{d,e}, Antoni Ruciński^d, Reinhard Schulte^c

^a*Centro de Ciências e Tecnologias Nucleares, Instituto Superior Técnico, Universidade de Lisboa, Estrada Nacional 10 (km 139,7), Bobadela LRS, 2695-066, Portugal*

^b*Departamento de Física, Instituto Superior Técnico, Universidade de Lisboa, Av. Rovisco Pais 1, Lisboa, 1049-001, Portugal*

^c*Department of Basic Science, Division of Biomedical Engineering Sciences, Loma Linda University, 201 Mortensen Hall, 11085 Campus St, Loma Linda, 92350, California, United States of America*

^d*Cyclotron Centre Bronowice, Institute of Nuclear Physics Polish Academy of Sciences, Radzikowskiego 152, Kraków, 31-342, Poland*

^e*Radiological Metrology and Biomedical Physics Division, National Centre for Nuclear Research, ul. Andrzeja Sołtana 7, Otwock Świerk, 05-400, Poland*

^f*Biomedical Physics Division, Institute of Experimental Physics, Faculty of Physics, University of Warsaw, 5 Pasteur Street, Warsaw, 02-093, Poland*

^g*GSI Helmholtzzentrum für Schwerionenforschung GmbH (GSI), Planckstr. 1, Darmstadt, 64291, Germany*

^h*Facility for Antiproton and Ion Research in Europe GmbH (FAIR), Planckstr. 1, Darmstadt, 64291, Germany*

Abstract

In recent years, compact nanodosimetric detectors based on ion multiplication in low-pressure gas have been developed and gained attention in the scientific community. These detectors use strong electric fields to collect and multiply positive ions produced by the incident radiation in mm-sized cell holes in dielectric materials, achieving a nm-equivalent spatial resolution of the localization of ionization events, when scaled to liquid water with unit density. Their design assumes that ion impact ionizations of gas molecules within the cell holes dominate signal formation, yet this assumption has lacked direct physical verification. Electron emission from the cell hole walls due to ion impact could also contribute, requiring alternative designs to optimize efficiency.

To investigate this, a nanodosimetric detector featuring a single cell hole with a diameter of 1.5 mm in a dielectric plate was developed. Ion collection and multiplication were achieved by applying a negative high voltage to the glass cathode 0.5 mm below the cell hole, assisted by a low drift field above the plate. A grounded readout electrode with a 0.8 mm hole covers the cell hole to prevent interactions of

*Prepared for submission to RADMEAS

*Corresponding author

Email address: victor.merza@tecnico.ulisboa.pt (Victor Merza)

collected ions with the hole walls. High signal yields in 1 mbar and 2 mbar propane gas were observed and indicated that ion impact ionizations of the gas molecules are indeed the primary mechanism for signal induction. The compact nanodosimeter setup was further modeled with Geant4-DNA and Garfield++ for deeper insight. The results of these studies are important for understanding and developing a new class of nanodosimeters with potential applications in particle therapy, radiation protection, space dosimetry, and particle physics.

Keywords: Nanodosimetry, particle track structure, GEM, THGEM, Geant4, Geant4-DNA, Garfield++

1. Introduction

Nanodosimetry aims to predict DNA damage frequency and complexity based on the track structure of ionizing particles, which shows the nanometric spatial distribution of excitations and ionizations in tissue (Rucinski et al., 2021; Conte et al., 2023; Faddegon et al., 2023). Ionizations are considered the dominant contributors to radiobiological effectiveness, either by generating diffusing radicals that induce indirect DNA damage or by directly ionizing the DNA molecule. In particular, when occurring in a clustered pattern with more than four ionizations within or near the DNA molecule, the probability of creating irreparable or lethal lesions becomes significant. The ionization cluster size, which is the number of ionizations produced by a primary particle and its secondaries in the considered nanometric volume, e.g., a DNA segment covering about 10-20 base pairs, is proportional to the DNA lesion cluster size. Nanodosimetric quantities specifying the spatial distribution of ionization events are measurable. Thus, by specifying the nanometric pattern of ionization clustering, nanodosimetric quantities can be used as an alternative descriptor of radiation quality that can be validated experimentally (Conte et al., 2017).

Nowadays, the measurement of nanodosimetric quantities is only feasible in low-pressure gases, and thus in nanometer-equivalent sensitive volumes (SV). There are only a few nanodosimeters developed in the 1990s and early 2000s that are still operational. These include the ion counter detector (Garty et al., 2002; Hilgers et al., 2015; Hilgers and Rabus, 2019; Hilgers et al., 2022), the LNL Startrack Counter (Nardo et al., 2002), and the Jet Counter (Pszona et al., 2000; Bantsar, 2010; Pietrzak et al., 2018; Bancer et al., 2020). Most recent research aimed to design compact track structure imaging detectors with nanometer-equivalent resolution (Bashkirov et al., 2009a,b; Casiraghi et al., 2014, 2015) or nanodosimeters (Vasi et al., 2021; Kempf and Schneider, 2025; Kempf et al., 2025), combining the working principle of thick gas electron multipliers (THGEM), and resistive plate chambers (RPC) operated at low-pressure and in reverse polarity. These compact detectors collect the positive ions produced by incident radiation from the SV and guide them into cell holes with diameters ranging from 0.8 mm to 2 mm in dielectric plates with thicknesses of 3 mm to 10 mm. In the cell hole, the collected ions generate a self-amplified signal (Fig. 1). Ion collection is achieved through a combination of a low drift field provided by an anode above the dielectric plate and a high-voltage cathode, which is attached to the bottom side of the plate and provides a strong electric field inside the cell hole. Due to the low diffusion of the ions, a nanometer-equivalent spatial

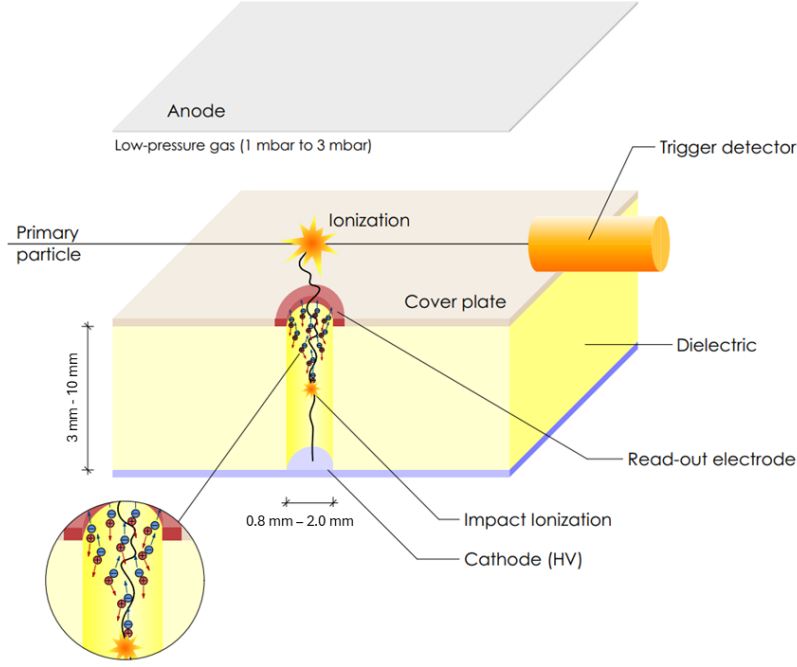


Figure 1: Illustration of the working principle of state-of-the-art compact nanodosimeters based on ion multiplication in low-pressure gas.

resolution of the starting position of the ions and thus the accurate 3D-localization of the ionizations can be achieved.

Although the efficiency of these detectors is not yet ready for practical applications, they are of great interest due to their potential for miniaturization. Miniaturized nanodosimeters could provide a tool in medical physics or radiation protection for the validation of nanodosimetry-based treatment plans or the characterization of radiation quality. Track structure imaging detectors based on such a technology would also be applicable in many fields in particle physics.

While the fundamental assumption regarding the working principle is that the signal is initiated through the impact ionization of gas molecules inside the cell holes by the accelerated positive ions, there is no experimental evidence to support this. It was hypothesized that ions hitting the cell walls could also release electrons and thus generate a signal. Assuming that ions hitting the cell hole walls are the dominant cause for signal creation, this would result in fundamentally different design optimization to maximize the probability of such events. On the contrary, if ion impact ionizations of the gas molecules are the dominant cause for signal creation, this would confirm the current assumption and also give important insights into the signal generation of the detector, allowing for further optimization. The goal of the measurements and simulations presented in this paper was to support further evidence that the signals produced in the detector are initiated through ion impact ionizations of the gas molecules in the strong electric field inside the cell hole. Our results indicate that, consistent with earlier assumptions, ion-impact ionization of the gas molecules is the predominant mechanism driving signal formation, rather than secondary electron emission from dielectric surfaces.

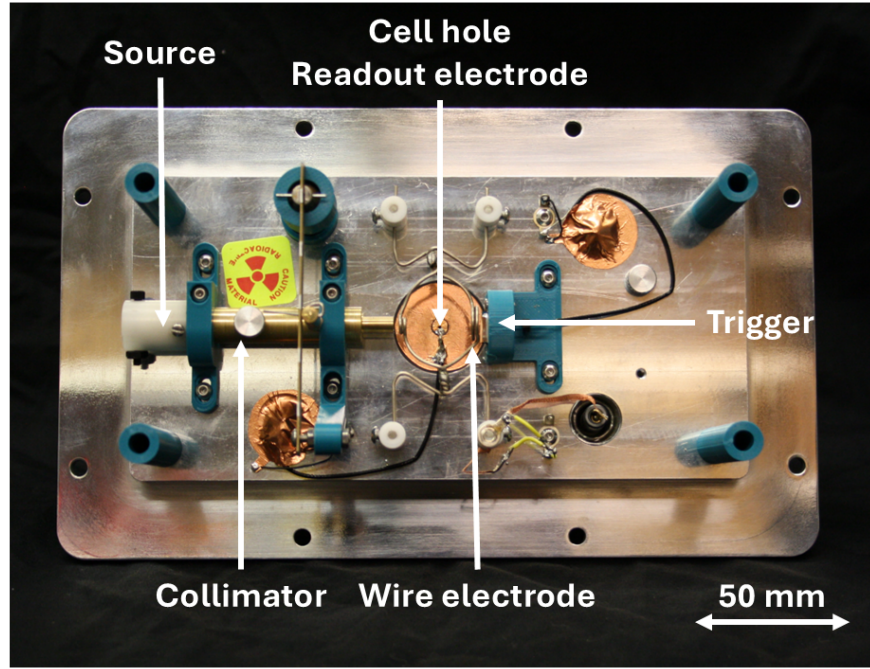


Figure 2: Top view of the detector interior attached to the lid of the low-pressure chamber.

2. Materials and Methods

2.1. Experimental Methods

2.1.1. Nanodosimeter Setup

The nanodosimetric prototype used in the measurements is shown in Fig. 2. It features a single hole with a diameter of 1.5 mm drilled in a 3 mm thick acrylic (polymethyl methacrylate, PMMA) dielectric plate (Fig. 3). On the top surface of the plate, which faces the low-pressure gas drift region traversed by the primary particles, a readout electrode made of copper foil is attached using non-conductive adhesive. The readout electrode, which features an outer diameter of 5 mm and a central circular opening with a diameter of 0.8 mm, is positioned concentrically with the cell hole. The remaining copper-foil-covered surface of the dielectric plate is not in contact with the readout electrode. A 0.7 mm thick low-resistive glass cathode measuring 12 mm \times 12 mm is attached to the bottom side of the dielectric plate. The bulk resistivity of the glass is of the order of 10^{10} Ω cm (Wang et al., 2019, 2010). An o-ring with an outer diameter of 9.6 mm and an inner diameter of 6 mm is used to seal the cathode to the dielectric plate's air side. Although there is a groove to embed this o-ring in the dielectric, a small gap of approximately 0.5 mm arises between the cathode and the plate. To ensure direct electrical contact between the cathode and the dielectric plate, two contacts made of conductive ink are applied on opposite sides of the air side of the o-ring.

A rectangular copper anode plate with dimensions of 80 mm \times 40 mm, positioned 20 mm above the readout electrode, provides the drift field. At a distance of 10 mm above the dielectric plate (halfway from the anode), a silver-cladded copper wire ring (30 mm in diameter) is suspended from the anode to ensure a uniform electric field distribution. A 1 mm collimated alpha-particle beam (see next paragraph) traverses

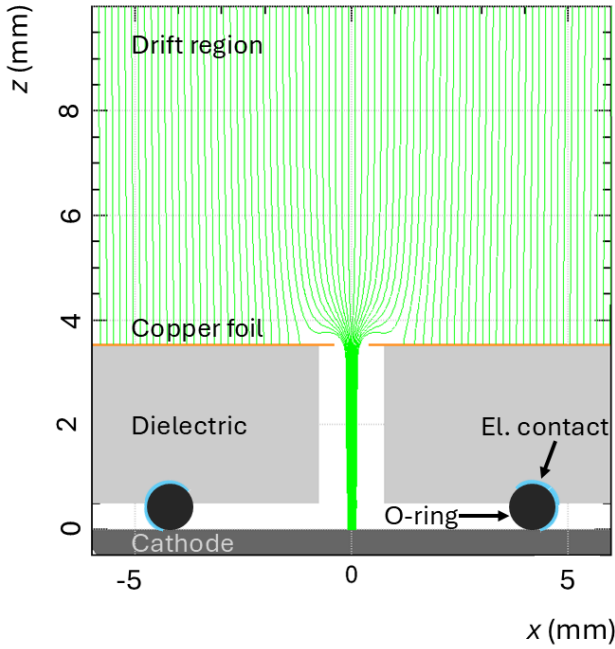


Figure 3: Schematic of the detector in the x - z plane, where the z -axis is normal to the dielectric plate and the x -axis is aligned with the alpha-particle beam axis. The sketch highlights the central axis of the circular hole in the dielectric plate and is superimposed with electric field streamlines generated by the cathode at -800 V and the anode, positioned at $z = 23.5$ mm (not shown), with a potential of 30 V.

the chamber at 10 mm above the dielectric plate. To allow unobstructed passage of the beam through the silver-clad copper wire ring, which is positioned at the same height, the wire forms a small loop around the beam path on either side. The central beam axis of the primary particle beam traversing the volume between the anode and the readout electrode passes directly above the center of the dielectric plate hole.

The Am-241 source (Eckert & Ziegler, catalog number AM1A2100U) emitting alpha particles with a mean energy of 4.6 MeV is attached to a brass collimator with a length of 80 mm at a distance of 95 mm from the cell hole axis. The beam-defining aperture of the collimator has a diameter of 1 mm. A PIN photodiode with a square sensitive area of 3.2 mm \times 3.2 mm, positioned 15 mm from the cell hole axis, registers primary particles at a rate of about 2.2 Hz and is used as the trigger detector.

The data acquisition system includes a digital Picoscope 3206D oscilloscope (Pico Technology Ltd., UK), picking up the signals, which are analyzed retrospectively. It is required to attenuate the nanodosimeter signal produced in the cell hole to a level suitable for an ORTEC 9301 preamplifier (ORTEC, Oak Ridge, Tennessee, USA) by terminating its input line with an additional 50 Ohm to ground. Further, a 6 dB attenuator is used right before the preamplifier's input. The trigger detector signals are amplified via a CAEN 1425 preamplifier (C.A.E.N. S.p.A., Viareggio, Italy). Both preamplifiers are connected to the oscilloscope input channels via 50 Ω terminators.

The gas system, providing a continuous gas flow in the low-pressure chamber of the nanodosimeter, consists of a 248A flow control valve (MKS Inc., Andover, MA, USA), an MKS Type 250 pressure/flow controller, an MKS Type 626 Baratron manometer, and a manual precision valve to adjust the outflow to the vacuum pump.

The measurements were performed in propane gas at room temperature, $(24 \pm 1)^\circ\text{C}$, at pressures of 1 mbar and 2 mbar, respectively. The cathode voltage ranged from -600 V to -1000 V, and was incrementally increased in 50 V steps. The anode voltage was fixed at 30 V, and the silver-cladded copper wire ring between the anode and the dielectric plate was at 15 V. The voltages were applied using an ORTEC 710 power supply.

2.1.2. Characterization of Detector Performance

The performance of the detector was characterized by the signal yield η , which is the ratio of the number of triggers with a subsequent nanodosimeter (ND) signal in timely coincidence and the total number of triggers. The time distribution of the delays between the maxima of the trigger signals and the following ND signals was recorded within a time window of $t = 200 \mu\text{s}$ after the registration of the trigger signal and fitted with a Gaussian function. It was established, as a convention, that an ND signal occurred in timely coincidence with a previous trigger signal if it was recorded within Δt_{arr} . The arrival time window Δt_{arr} was defined as the $\pm 3 \sigma$ interval of the Gaussian fit.

The number N_{trigger} of registered triggers, the number N_{coinc} of ND signals that occurred within Δt_{arr} , and the number $N_{\text{no coinc}}$ outside of Δt_{arr} , but within t , was determined. To ensure conservatism in the calculation of the signal yield, $N_{\text{no coinc}}$ was excluded from the calculation of the signal yield. The signal yield η was then calculated as follows:

$$\eta = \frac{N_{\text{coinc}}}{N} \quad (1)$$

2.2. Detector Simulations

The computational modeling of the conducted experiments included:

- Radiation transport simulations using the condensed history Monte Carlo code Geant4 (Allison et al., 2016, 2006; Agostinelli et al., 2003) and track structure modeling using Geant4-DNA (Tran et al., 2024; Incerti et al., 2018; Bernal et al., 2015; Incerti et al., 2010b,a)
- Electrostatic field simulations using the finite element method software Elmer (Malinen and Råback, 2013)
- Ion drift simulations using the detector simulation toolkit Garfield++ (Schindler, 2025)

The computational methods for compact nanodosimeter simulations are only briefly described here as they have been described and discussed in more detail in our previous publication (Merza et al., 2025).

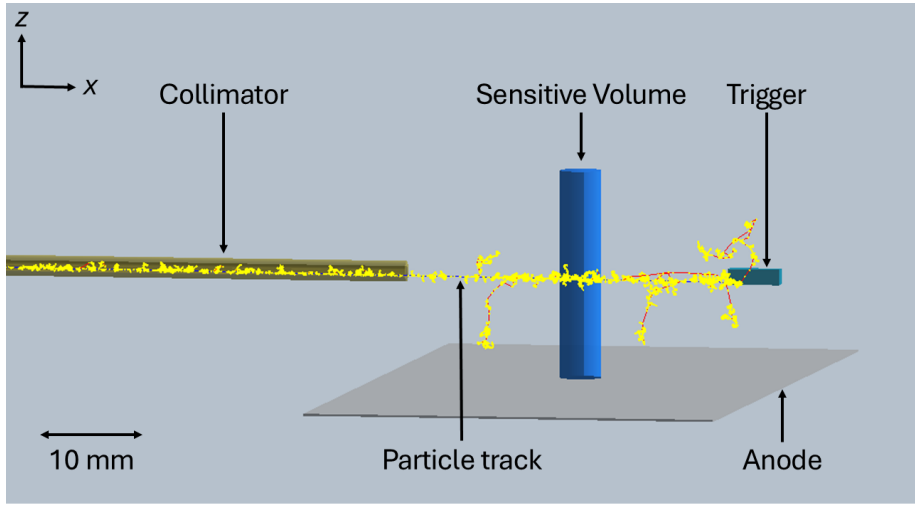


Figure 4: Simplified Geant4 model of the experimental setup. The collimator is simplified, only showing the central gas-filled hole and a thin layer of brass surrounding it. The walls of the low-pressure chamber are not shown for better visibility.

2.2.1. Track Structure and ICSD Simulation

The simplified Geant4 model included the walls of the low-pressure chamber made of aluminum, an infinitely thin disk-shaped monoenergetic 4.6 MeV alpha source attached to the collimator, the trigger detector, and the copper anode (Fig. 4). Interior detector parts that were assumed not to influence the radiation transport, e.g., holders or electrodes outside of the beam, were not included in this model.

Using the `G4EMLivermorePhysics` list, the radiation transport was simulated in all volumes except for the low-pressure gas. Geant4-DNA option 4 was chosen for the track structure simulation and the determination of the ionization cluster size distribution (ICSD), which is the frequency distribution of the ionization cluster size, in the SV (see Sec. 2.2.3). The positions of the ionizations in the drift region between the anode and the dielectric plate were recorded. Since there were no available cross-section data of alpha particles in propane available in Geant4-DNA, a density scaling procedure (Grosswendt, 2004; Grosswendt et al., 2004) was applied to mimic the propane gas using liquid water, taking into account the different mean free path length with respect to ionization compared to that in propane. Accordingly, the density ρ_{water} of the liquid water is:

$$\rho_{\text{water}} = \rho_{\text{propane}} \cdot \frac{(\lambda\rho)_{\text{water}}^{\text{ion}}}{(\lambda\rho)_{\text{propane}}^{\text{ion}}} \quad (2)$$

ρ_{propane} is the density of propane at the corresponding pressure applied in the experiment. The ratio of the mean free path lengths of water and propane with respect to ionization, $(\lambda\rho)_{\text{water}}^{\text{ion}}/(\lambda\rho)_{\text{propane}}^{\text{ion}} \approx 1.45$, is nearly energy-independent (Grosswendt, 2004).

2.2.2. Electric Field Simulation

For the calculation of the electrostatic fields with Elmer, a simplified geometrical model of the active detector part consisting of the cathode, dielectric plate, readout

electrode, drift region, and anode was modeled. The influence of the collimator, the detector walls, and the trigger detector on the electric field was not taken into account. The permittivity of the acrylic was set to 2.7.

2.2.3. Ion Drift Simulation and Sensitive Volume Definition

Garfield++ simulations of the ion drift trajectories of single-ionized propane molecules (C_3H_8^+) in the electrostatic fields were performed using ion mobility values published in (Kempf and Schneider, 2024). For each setup, i.e., the chosen combination of gas pressure and cathode voltage, the ion drift trajectories were calculated from the points of ionization simulated with Geant4-DNA (see above). Ion starting positions were restricted to a cylindrical region, the sensor region, with a diameter of 30 mm and a height of 20 mm, extending from the top surface of the dielectric plate to the anode. To get about 10^5 starting ions in the sensor region, 10^4 primary alpha particles were simulated. The ion trajectory simulation was terminated when the ion reached any solid part of the detector, and the coordinates of its endpoint were recorded. An ion was considered collected if it passed through the opening of the cell hole.

To define the SV of the detector, which is required for the calculation of an ICSD using Geant4-DNA, the radial ion collection efficiency was determined. The sensor region was divided into 300 concentric radial bins of width 0.05 mm. For each bin, the ion collection efficiency was calculated as the ratio of ions collected to ions initially placed in that radial bin. Consistent with our previous work (Merza et al., 2025), which showed weak dependence of the ion collection efficiency on the vertical start position of the ion above the dielectric plate, efficiencies were averaged over the vertical coordinate within the sensor region to yield a radial profile. This profile was interpolated using a cubic spline. The SV was then defined as a cylinder whose radius corresponds to the radial distance at which the interpolated collection efficiency falls to $1/e$.

2.3. Estimation of the signal creation probability

The signal creation probability p_s for each collected ion was estimated using the measured signal yield η (see Sec. 2.1.2) together with the Garfield++-simulated number of collected ions per trigger (see Sec. 2.2.3). As a first approximation, p_s can be inferred from the probability that no signal is produced over N triggers:

$$1 - \eta = \frac{1}{N} \sum_{i=1}^N (1 - p_s)^{n_i} \quad (3)$$

Here, N denotes the total number of primary particles, and n_i is the number of collected ions simulated for the i^{th} primary particle using Garfield++. Eq. 3 was solved numerically using the Python function `fsolve` to determine the value of p_s .

3. Results

3.1. Track Structure and Ion Collection from the Sensitive Volume

Fig. 5 shows an example for the Geant4-DNA simulated ICSD produced in the SV at 1 mbar propane gas pressure for -800 V cathode voltage. This ICSD has a

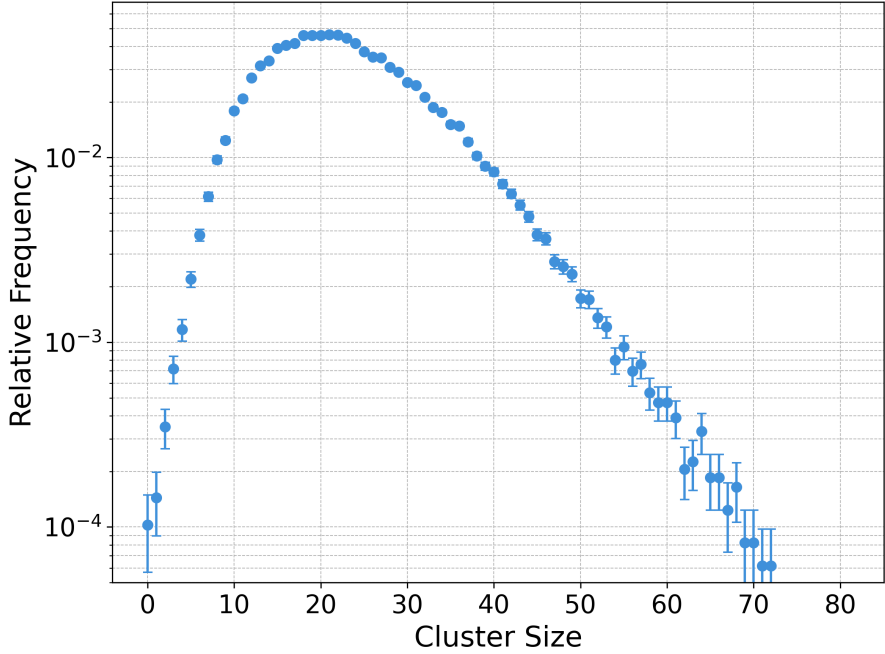


Figure 5: Geant4-DNA simulated ICSD produced in the SV with a diameter of 3.09 mm for a cathode voltage of -800 V and a propane gas pressure of 1 mbar.

maximum at a cluster size of around 20 and rapidly falls off for higher and smaller cluster sizes, respectively. The relative probability for zero ionizations produced in the SV is lower than $\lesssim 10^{-4}$ for all configurations.

Tab. 1 lists the SV sizes, the mean cluster sizes M_1 derived from the ICSD, and the Garfield++ simulated mean number N_{coll} of ions collected in the cell hole per incident primary alpha particle for each detector configuration. Equivalent SV sizes in nm correspond to the size of the SV when scaled to liquid water with unit density according to Eq. 2. The highest M_1 of about 58 was obtained for the propane pressure of 2 mbar and cathode voltage of -1000 V. Note that N_{coll} represents the mean simulated number of collected ions in the static field.

Another important characteristic of the track structure is the radial distribution of ionizations around the central beam axis of the incident primary particle beam, which directly affects the ion arrival time spectrum. At the pressures applied in this work (1 mbar and 2 mbar), secondary and higher-order delta electrons can travel up to a few mm from their point of origin before they reach a sub-ionization threshold. Fig. 6 shows the Geant4-DNA simulated ionization density in the drift region above the cell hole, which shows a strong decrease with radial distance from the central beam axis. The plateau towards lower radial distance is due to the collimation of the beam.

3.2. Arrival Time Spectra and Electric Field Distribution

Fig. 7 shows the average ion arrival time measured as a function of the cathode voltage. A decrease in the mean ion arrival time was observed with increasing cathode voltage. Detailed results, including the standard deviation σ and the coefficient of determination R^2 of the Gaussian fits to the measured ion arrival time

p (mbar)	U_{Cath} (V)	d_{SV} (mm)	$d_{\text{SV}}^{\text{equ}}$ (nm)	M_1	N_{coll}
1	-600	2.81	6.90	20.87(8)	16.82(7)
	-650	2.93	7.20	22.00(9)	17.51(7)
	-700	2.94	7.23	22.13(9)	18.08(7)
	-750	3.00	7.37	22.68(9)	18.70(7)
	-800	3.09	7.58	23.46(9)	19.29(7)
	-850	3.11	7.63	23.65(9)	19.83(8)
	-900	3.17	7.78	24.21(9)	20.37(8)
	-950	3.23	7.93	24.78(9)	20.94(8)
	-1000	3.31	8.13	25.55(9)	21.43(8)
	-600	2.82	13.88	48.66(24)	38.94(18)
2	-650	2.91	14.29	50.46(24)	40.50(19)
	-700	2.95	14.48	50.10(25)	41.79(20)
	-750	3.03	14.91	53.09(25)	43.36(20)
	-800	3.08	15.16	54.14(25)	44.74(20)
	-850	3.12	15.34	54.96(26)	46.01(21)
	-900	3.18	15.64	56.21(26)	47.21(21)
	-950	3.24	15.93	57.44(26)	48.48(22)
	-1000	3.28	16.13	58.3(27)	49.56(22)

Table 1: Diameters d_{SV} of the SV in the low-pressure gas, their equivalents $d_{\text{SV}}^{\text{equ}}$ in liquid water with unit density, as well as the mean cluster size M_1 and the simulated mean number N_{coll} of collected ions for the stated gas pressures p and cathode voltages U_{Cath} .

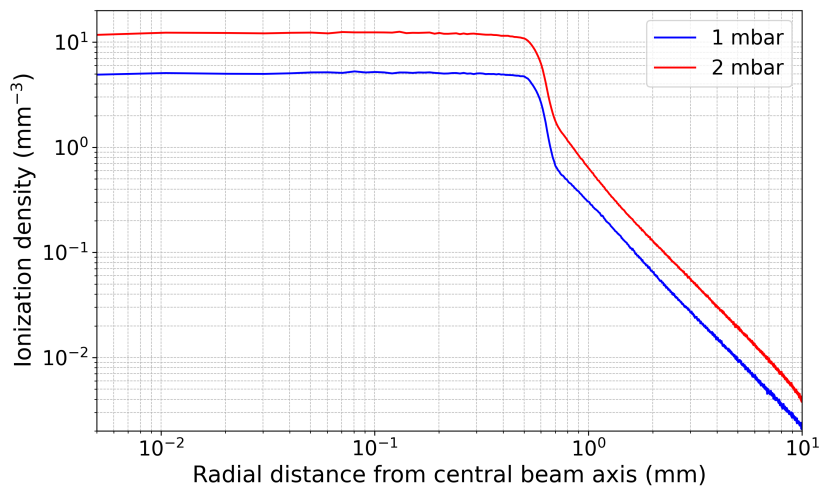


Figure 6: Geant4-DNA simulated ionization density as a function of the radial distance of the central beam axis of the collimated beam of 4.6 MeV alpha particles for the stated propane gas pressures.

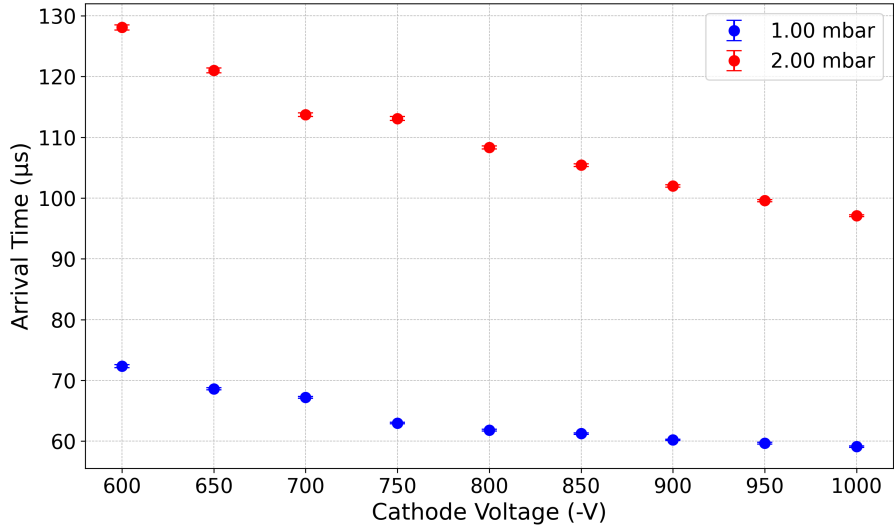


Figure 7: Mean measured ion arrival time as a function of the cathode voltage for the stated propane gas pressures.

distributions, are summarized in Tab. 2.

As discussed in the previous section, due to the low pressure of the gas, the radial distance of ionizations from the central beam axis reached the mm range. The initial ion positions in the drift region were distributed accordingly, determining the width of the ion arrival time spectra. Additionally, ion diffusion in the gas broadened the arrival time distribution.

In Fig. 8, the calculated electric field magnitudes along the z -axis of the cell hole are presented for different cathode voltages. In the drift region, the contribution of the penetrating field generated by the cathode becomes apparent at about 2 mm above the hole. The electric field magnitude increases rapidly in the vicinity of or inside the cell hole and reaches its maximum value at the cathode.

All ion drift trajectories simulated using Garfield++ terminated either on the readout electrode, the surrounding copper-covered area, or at the cathode. No ion impacts on the cell hole walls were observed in the simulation.

3.3. Signal Yield

Either no signal or only one signal per registered primary alpha particle was observed within the time window of 200 μ s following each trigger. Only a maximum of 2 % for 1 mbar, and 3 % for 2 mbar of observed signals occurred outside of the defined arrival time window. Fig. 9 shows the measured signal yield of the detector as a function of the applied cathode voltage, for 1 mbar and 2 mbar propane gas pressure, respectively, calculated according to Eq. 1. The signal yield increased almost linearly with the applied cathode voltage, both for 1 mbar and 2 mbar. The highest signal yield amounted to about 52 % at 1 mbar and 41 % at 2 mbar. For cathode voltages higher than -1000 V, the detector operation became unstable.

3.4. Signal Creation Probability

Fig. 10 shows the signal creation probability, calculated according to Eq. 3, as a function of the cathode voltage for 1 mbar and 2 mbar propane gas pressure. It

p (mbar)	U_{Cath} (V)	$t_{\text{arr}}^{\text{meas}}$ (μs)	R^2	σ (μs)
1	-600	72.36(26)	0.985	7.87
	-650	68.62(17)	0.993	7.46
	-700	67.23(16)	0.994	7.36
	-750	63.07(14)	0.993	7.27
	-800	61.82(13)	0.994	6.96
	-850	61.26(12)	0.992	7.17
	-900	60.23(11)	0.994	7.21
	-950	59.68(15)	0.996	7.26
	-1000	59.11(11)	0.994	6.99
	-600	128.1(4)	0.965	13.59
2	-650	121.0(4)	0.972	13.66
	-700	113.7(3)	0.977	12.61
	-750	113.1(3)	0.978	12.49
	-800	108.36(25)	0.989	12.16
	-850	105.43(23)	0.987	12.06
	-900	101.99(21)	0.987	11.65
	-950	99.58(16)	0.992	11.30
	-1000	97.12(15)	0.992	11.26

Table 2: Mean measured ion arrival times $t_{\text{arr}}^{\text{meas}}$ as a function of the cathode voltage U_{Cath} for the stated gas pressures p . The coefficient of determination R^2 and the standard deviation σ characterize the Gaussian fit of the measured data.

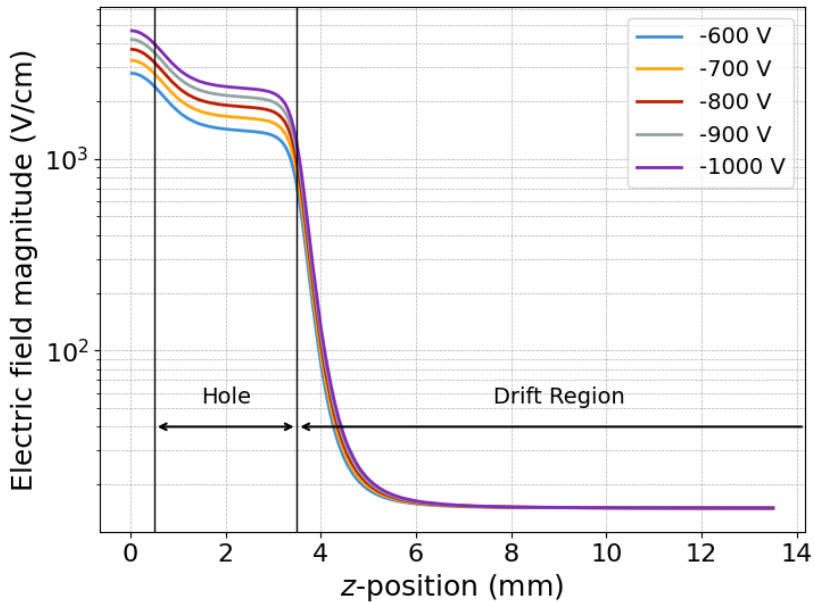


Figure 8: Simulated electric field magnitude for different cathode voltages along the z -axis, which runs centrally through the hole. The central beam axis was at $z = 13.5$ mm, the dielectric plate at $z = [0.5 \text{ mm}, 3.5 \text{ mm}]$, and the cathode at $z = 0$ mm.

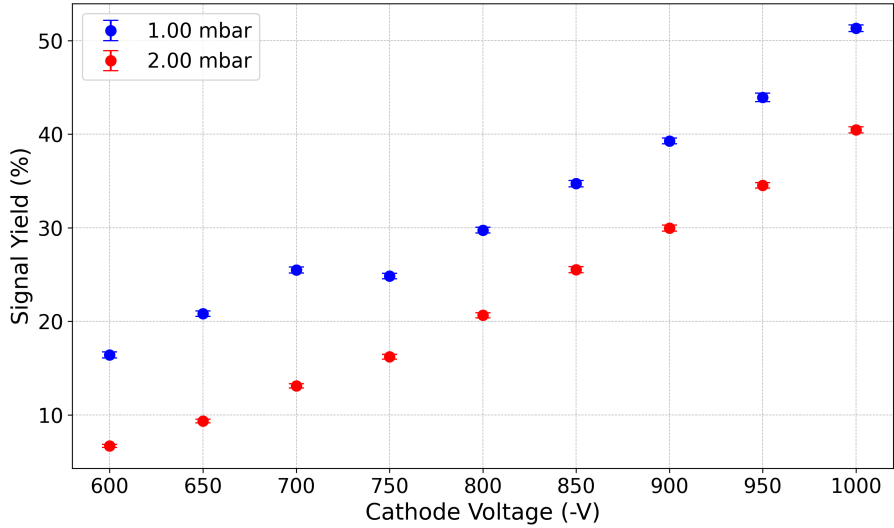


Figure 9: Measured signal yields as a function of the cathode voltage for the stated propane gas pressures.

increases with increasing cathode voltage and reaches maximum values of 3.5 % for 1 mbar and 1.1 % for 2 mbar.

4. Discussion

The compact nanodosimeter prototype signal yield depends strongly on the applied cathode voltage, i.e., it increases with the cathode voltage to up to 52 % for 1 mbar and 41 % for 2 mbar propane gas pressure at a cathode voltage of 1000 V, respectively. It thus reaches values comparable to other nanodosimetric prototypes based on the same working principle, like the FIRE (Vasi et al., 2021) or the FIRE-V2 (Kempf et al., 2025) detectors despite the comparatively small dielectric plate thickness of 3 mm for our detector. Even higher signal yields may be anticipated for cathode voltages exceeding -1000 V. Therefore, current efforts are focusing on achieving a stable detector operation at these higher voltages. Since the probability for zero ionizations produced in the SV was negligible for all detector configurations according to the Geant4-DNA simulations, it was justified to calculate the signal yield without a correction factor for zero ionizations.

Besides the higher electric field magnitude itself, another contribution to the higher measured signal yields observed at increased cathode voltages is the greater number of ions collected from the SV. Due to the penetrating electric field predicted by Elmer, it can be assumed that ion impact ionizations also occur above the cell hole. The ions produced there may be collected in the cell hole and subsequently produce a measurable signal.

Comparing the Garfield++-simulated number of collected ions with the experimentally measured signal yield suggests that, under the assumption that only ion-impact ionization of gas molecules is responsible for signal creation (see discussion below), the signal creation probability per collected ion did not exceed the low single-digit percent range. This could be increased, for instance, by applying higher

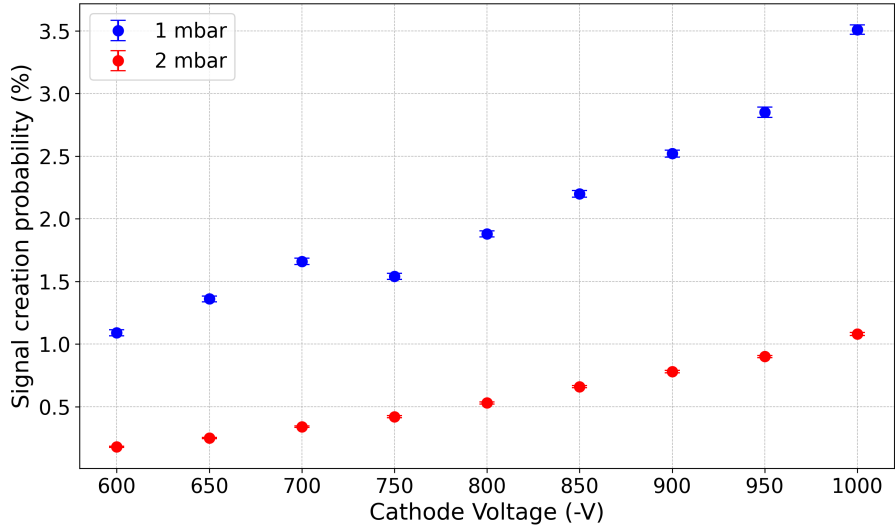


Figure 10: Signal creation probability per collected ion as a function of the cathode voltage for the stated propane gas pressures.

cathode voltages, combined with increased dielectric plate thickness, or selecting an alternative working gas, and reducing upcharging of the dielectric.

In addition to the low efficiency of the ion impact ionization, the fact that no more than a single signal was observed per trigger points to a dead time longer than the measurement time window per trigger of 200 μ s. The most likely reasons for this long dead time are the persistence of the ion cloud after the discharge and upcharging of the cell hole walls. Measures to reduce this dead time are underway.

Garfield++ simulations indicated that the ion drift trajectories were concentrated in the center of the cell hole; thus, a significant contribution of ion-wall interactions on the signal yield can practically be excluded for the geometry of the hole used in the experimental setup. However, it was not possible to accurately model the ion arrival time spectra and the positions of the ion impact ionization with Garfield++ due to the lack of data on the ion impact ionization cross sections. That could, once available, easily be implemented in Garfield++.

In principle, ion-induced secondary electron emission (IISEE) from the cathode could also contribute to signal creation. In IISEE, both the kinetic energy of the incoming propane ion and its residual potential energy must be considered. The kinetic energy of the collected ions at the cathode is of the order of a few tens of eV. Typically, energies in the keV range are required for IISEE through the kinetic emission process. Therefore, this effect was excluded.

For IISEE through the transfer of potential energy, the potential energy stored must be at least two times larger than the energy barrier required for electron release. Since the ionization potential of C_3H_8^+ -ions is 11.1 eV, an energy barrier of less than about 5.55 eV would be required to allow IISEE through this mechanism. Depositions or impurities on the cathode surface, which were reported in previous studies (Vasi et al., 2021), including monolayers of foreign molecules, could influence the IISEE yield. However, it would tend to result in even lower electron yields (Arazi, 2018). The few studies on IISEE yields of insulating materials found in the literature

suggested negligibly low ISEE yields for glass (van Elsbergen et al., 2000), or other insulators (Kim et al., 2000; Barnard et al., 1997) in the energy range relevant for our application; however, these measurements were not performed using propane ions. Experimental data found in the literature on insulators suggest a generally lower ISEE yield of molecular ions and in gases other than noble gases (Vance, 1968a,b). Based on the data available in the literature, there is no significant contribution to the signal yield from ISEE.

5. Conclusion

In this work, an alternative design of a compact nanodosimetric detector has been presented. The combination of a large cell hole with a small ion-focusing readout electrode minimizes the possibility of ion-wall interactions inside the detector's cell hole. The observed signal yield strongly indicates that ion-impact ionization of the gas molecules within the cell hole is the dominant mechanism, driving signal formation in this detector. However, the probability for an individual ion to produce a detectable signal remains in the single-percentage range. The results underline the crucial role of reliable ion impact ionization cross-section data for the continued development and accurate modeling of detectors based on ion multiplication in low-pressure gas. This development is expected to continue in the future.

6. Author statement

Victor Merza: Writing - Original Draft, Methodology, Conceptualization, Software. **Aleksandr Bancer:** Conceptualization, Resources. **Vladimir Bashkirov:** Conceptualization, Methodology. **Ana Belchior:** Supervision. **Beata Brzozowska:** Writing - Review & Editing, Methodology, Project administration. **João F. Canhoto:** Writing - Review & Editing. **Piotr Gasik:** Writing - Review & Editing, Methodology. **Jarosław Grzyb:** Methodology, Resources. **Khaled Katmeh:** Writing - Review & Editing. **Marcin Pietrzak:** Writing - Review & Editing, Methodology, Software. **Antoni Ruciński:** Supervision, Project administration. **Reinhard Schulte:** Writing - Review & Editing, Conceptualization, Supervision.

7. Data statement

All data can be provided by the corresponding author upon request.

8. Acknowledgements

This work was partially funded by the Fundação para a Ciência e a Tecnologia (FCT) through the research grants PRT/BD/153748/2021, PRT/BD/151544/2021, and PRT/BD/153750/2021. Further, financial support was received by the National Science Centre, Poland, under the grant number UMO-024/06/Y/ST2/00196. The authors gratefully acknowledge the support of Ingo Deppner (GSI), who kindly provided the low-resistivity glass used in this work.

Appendix A. Experimental and Simulation Uncertainties

The stated uncertainties in the Results are equal to the standard uncertainties of the quantities as discussed below. A coverage factor of $k = 1$ was used, which corresponds to a confidence interval of 68 % (JCGM, 2023).

Appendix A.1. Experimental Signal Yield

The signal yield η was calculated as stated in Eq. 1. N is the number of primary particles registered by the trigger, t is the time window opened after each trigger in which signals were recorded, and N_{coinc} is the number of signals recorded within the arrival time window t_{arr} . Of note, during our experiments, only one or no ND signal was recorded within the time window t following a trigger. The partial derivative of η with respect to N_{coinc} is

$$\frac{d\eta}{dN_{\text{coinc}}} = \frac{1}{N} \quad (\text{A.1})$$

Assuming a binomial distribution of N_{coinc} , the variance of N_{coinc} is given by

$$\sigma_{N_{\text{coinc}}}^2 = N \cdot \eta \cdot (1 - \eta) \quad (\text{A.2})$$

Applying the Gaussian error propagation, the standard uncertainty u_η of η thus resulted in

$$u_\eta = \sqrt{\left(\frac{d\eta}{dN_{\text{coinc}}}\right)^2 \cdot \sigma_{N_{\text{coinc}}}^2} = \sqrt{\frac{\eta \cdot (1 - \eta)}{N}} \quad (\text{A.3})$$

Appendix A.2. Simulated ICSD

The standard uncertainty u_{M_1} of the mean cluster size M_1 of the presented ICSD is given by

$$u_{M_1} = \frac{\sigma_\nu}{\sqrt{N}} \quad (\text{A.4})$$

where σ_ν is the standard deviation of the cluster size ν and N is the total number of starting primary particles that produced that ICSD. The standard uncertainty u_{p_ν} of the individual probability p_ν of the cluster size ν is given by

$$u_{p_\nu} = \sqrt{\frac{\nu}{N}} \quad (\text{A.5})$$

Appendix A.3. Estimated Signal Creation Probability

Since Eq. 3 is a nonlinear relation with respect to the signal creation probability p_s , implicit differentiation is required to obtain the standard uncertainty u_{p_s} of p_s . We define the function $f(p_s(\eta, n_i))$:

$$f(p_s(\eta, n_i)) = \frac{1}{N} \cdot \sum_{i=1}^N (1 - p_s)^{n_i} - (1 - \eta) = 0 \quad (\text{A.6})$$

In the following, we leave the functional dependence of $f(p_s(\eta, n_i))$ implicit for better readability. Further, we use the short-hand notation $S = \frac{1}{N} \cdot \sum_{i=1}^N n_i \cdot (1 - p_s)^{n_i-1}$. The partial derivatives of p_s with respect to η and n_i result in:

$$\frac{\partial p_s}{\partial \eta} = -\frac{\partial f / \partial \eta}{\partial f / \partial p_s} = \frac{1}{S} \quad (\text{A.7})$$

and, approximating the discrete Poisson-distributed n_i as a continuous function,

$$\frac{\partial p_s}{\partial n_i} = -\frac{\partial f/\partial n_i}{\partial f/\partial p_s} = \frac{(1-p_s)^{n_i} \cdot \ln(1-p_s)}{N \cdot S} \quad (\text{A.8})$$

According to the Gaussian error propagation law, the combined standard uncertainty u_{p_s} is given by:

$$u_{p_s} = \sqrt{\left(\frac{\partial p_s}{\partial \eta}\right)^2 \cdot u_\eta^2 + \sum_{i=1}^N \left(\frac{\partial p_s}{\partial n_i}\right)^2 \cdot u_{n_i}^2} \quad (\text{A.9})$$

The standard uncertainty u_{n_i} of the Poisson-distributed simulated number n_i of collected ions for each primary particle, which was obtained from the Garfield++ simulation, is given by $u_{n_i} = \sqrt{n_i}$. The standard uncertainty u_{n_η} was determined in Sec. Appendix A.1. Finally, u_{p_s} results in

$$u_{p_s} = \sqrt{\frac{1}{S^2} \cdot u_\eta^2 + \sum_{i=1}^M \frac{(1-p_s)^{2n_i} \cdot (\ln(1-p_s))^2}{M^2 \cdot S^2} \cdot n_i} \quad (\text{A.10})$$

Appendix A.4. Other Experimental and Simulated Quantities

For the additional experimental and simulated quantities determined in this work, e.g., the measured ion arrival time or the simulated number of ions collected in the cell hole, the stated uncertainty represents the standard uncertainty u of the mean value of the quantity, which is given by

$$u = \frac{\sigma}{\sqrt{N}} \quad (\text{A.11})$$

where σ is the standard deviation and N is the number of measured or simulated samples.

References

Agostinelli, S., Allison, J., Amako, K., Apostolakis, J., Araujo, H., Arce, P., Asai, M., Axen, D., Banerjee, S., Barrand, G., Behner, F., Bellagamba, L., Boudreau, J., Broglia, L., Brunengo, A., Burkhardt, H., Chauvie, S., Chuma, J., Chytracek, R., Cooperman, G., Cosmo, G., Degtyarenko, P., Dell'Acqua, A., Depaola, G., Dietrich, D., Enami, R., Feliciello, A., Ferguson, C., Fesefeldt, H., Folger, G., Foppiano, F., Forti, A., Garelli, S., Giani, S., Giannitrapani, R., Gibin, D., Gómez Cadenas, J., González, I., Gracia Abril, G., Greeniaus, G., Greiner, W., Grichine, V., Grossheim, A., Guatelli, S., Gumplinger, P., Hamatsu, R., Hashimoto, K., Hasui, H., Heikkinen, A., Howard, A., Ivanchenko, V., Johnson, A., Jones, F., Kallenbach, J., Kanaya, N., Kawabata, M., Kawabata, Y., Kawaguti, M., Kelner, S., Kent, P., Kimura, A., Kodama, T., Kokoulin, R., Kossov, M., Kurashige, H., Lamanna, E., Lampén, T., Lara, V., Lefebure, V., Lei, F., Liendl, M., Lockman, W., Longo, F., Magni, S., Maire, M., Medernach, E., Minamimoto, K., Mora de Freitas, P., Morita, Y., Murakami, K.,

Nagamatu, M., Nartallo, R., Nieminen, P., Nishimura, T., Ohtsubo, K., Okamura, M., O’Neale, S., Oohata, Y., Paech, K., Perl, J., Pfeiffer, A., Pia, M., Ranjard, F., Rybin, A., Sadilov, S., Di Salvo, E., Santin, G., Sasaki, T., Savvas, N., Sawada, Y., Scherer, S., Sei, S., Sirotenko, V., Smith, D., Starkov, N., Stoecker, H., Sulkimo, J., Takahata, M., Tanaka, S., Tcherniaev, E., Safai Tehrani, E., Tropeano, M., Truscott, P., Uno, H., Urban, L., Urban, P., Verderi, M., Walkden, A., Wander, W., Weber, H., Wellisch, J., Wenaus, T., Williams, D., Wright, D., Yamada, T., Yoshida, H., Zschiesche, D., 2003. Geant4—a simulation toolkit. Nuclear Instruments and Methods in Physics Research Section A: Accelerators, Spectrometers, Detectors and Associated Equipment 506, 250–303. URL: <https://www.sciencedirect.com/science/article/pii/S0168900203013688>, doi:[https://doi.org/10.1016/S0168-9002\(03\)01368-8](https://doi.org/10.1016/S0168-9002(03)01368-8).

Allison, J., Amako, K., Apostolakis, J., Araujo, H., Arce Dubois, P., Asai, M., Barrand, G., Capra, R., Chauvie, S., Chytracek, R., Cirrone, G., Cooperman, G., Cosmo, G., Cuttome, G., Daquino, G., Donszelmann, M., Dressel, M., Folger, G., Foppiano, F., Generowicz, J., Grichine, V., Guatelli, S., Gumlplinger, P., Heikkinen, A., Hrivnacova, I., Howard, A., Incerti, S., Ivanchenko, V., Johnson, T., Jones, F., Koi, T., Kokoulin, R., Kossov, M., Kurashige, H., Lara, V., Larsson, S., Lei, F., Link, O., Longo, F., Maire, M., Mantero, A., Mascialino, B., McLaren, I., Mendez Lorenzo, P., Minamimoto, K., Murakami, K., Nieminen, P., Pandola, L., Parlati, S., Peralta, L., Perl, J., Pfeiffer, A., Pia, M., Ribon, A., Rodrigues, P., Russo, G., Sadilov, S., Santin, G., Sasaki, T., Smith, D., Starkov, N., Tanaka, S., Tcherniaev, E., Tome, B., Trindade, A., Truscott, P., Urban, L., Verderi, M., Walkden, A., Wellisch, J., Williams, D., Wright, D., Yoshida, H., 2006. Geant4 developments and applications. IEEE Transactions on Nuclear Science 53, 270–278. doi:[10.1109/TNS.2006.869826](https://doi.org/10.1109/TNS.2006.869826).

Allison, J., Amako, K., Apostolakis, J., Arce, P., Asai, M., Aso, T., Bagli, E., Bagulya, A., Banerjee, S., Barrand, G., Beck, B., Bogdanov, A., Brandt, D., Brown, J., Burkhardt, H., Canal, P., Cano-Ott, D., Chauvie, S., Cho, K., Cirrone, G., Cooperman, G., Cortés-Giraldo, M., Cosmo, G., Cuttome, G., Depaola, G., Desorgher, L., Dong, X., Dotti, A., Elvira, V., Folger, G., Francis, Z., Galoyan, A., Garnier, L., Gayer, M., Genser, K., Grichine, V., Guatelli, S., Guèye, P., Gumlplinger, P., Howard, A., Hřivnáčová, I., Hwang, S., Incerti, S., Ivanchenko, A., Ivanchenko, V., Jones, F., Jun, S., Kaitaniemi, P., Karakatsanis, N., Karamitros, M., Kelsey, M., Kimura, A., Koi, T., Kurashige, H., Lechner, A., Lee, S., Longo, F., Maire, M., Mancusi, D., Mantero, A., Mendoza, E., Morgan, B., Murakami, K., Nikitina, T., Pandola, L., Paprocki, P., Perl, J., Petrović, I., Pia, M., Pokorski, W., Quesada, J., Raine, M., Reis, M., Ribon, A., Ristić Fira, A., Romano, F., Russo, G., Santin, G., Sasaki, T., Sawkey, D., Shin, J., Strakovský, I., Taborda, A., Tanaka, S., Tomé, B., Toshito, T., Tran, H., Truscott, P., Urban, L., Uzhinsky, V., Verbeke, J., Verderi, M., Wendt, B., Wenzel, H., Wright, D., Wright, D., Yamashita, T., Yarba, J., Yoshida, H., 2016. Recent developments in geant4. Nuclear Instruments and Methods in Physics Research Section A: Accelerators, Spectrometers, Detectors and Associated Equipment

835, 186–225. URL: <https://www.sciencedirect.com/science/article/pii/S0168900216306957>, doi:<https://doi.org/10.1016/j.nima.2016.06.125>.

Arazi, L., 2018. On the possibility of positive-ion detection in gaseous tpcs and its potential use for neutrinoless double beta decay searches in ^{136}xe . *Journal of Physics: Conference Series* 1029, 012004. URL: <https://doi.org/10.1088/1742-6596/1029/1/012004>, doi:10.1088/1742-6596/1029/1/012004.

Bancer, A., Pietrzak, M., Mietelska, M., 2020. Particle track structure measurements from 0.5 to 18 nm in nitrogen using the jet counter nanodosimeter. *Radiation Physics and Chemistry* 172, 108805. URL: <https://www.sciencedirect.com/science/article/pii/S0969806X19308126>, doi:<https://doi.org/10.1016/j.radphyschem.2020.108805>.

Bantsar, A., 2010. Ionization Cluster Size Distributions Created by Low Energy Electrons and Alpha Particles in Nanometric Track Segment in Gases. Ph.D. thesis. Soltan Inst., Swierk. [arXiv:1207.6893](https://arxiv.org/abs/1207.6893).

Barnard, J., Bojko, I., Hilleret, N., 1997. Measurements of the Secondary Electron Emission of Some Insulators. Technical Report. European Laboratory for Particle Physics CERN-LHC Division. URL: <https://cds.cern.ch/record/1514931/files/arxiv:1302.2333.pdf>.

Bashkirov, V., Schulte, R., Wroe, A., Sadrozinski, H., Gargioni, E., Grosswendt, B., 2009a. Experimental validation of track structure models. *IEEE Transactions on Nuclear Science* 56, 2859–2863. doi:10.1109/TNS.2009.2029574.

Bashkirov, V.A., Hurley, R.F., Schulte, R.W., 2009b. A novel detector for 2d ion detection in low-pressure gas and its applications, in: 2009 IEEE Nuclear Science Symposium Conference Record (NSS/MIC), pp. 694–698. doi:10.1109/NSSMIC.2009.5402061.

Bernal, M.A., Bordage, M.C., Brown, J.M.C., Davídková, M., Delage, E., El Bitar, Z., Enger, S.A., Francis, Z., Guatelli, S., Ivanchenko, V.N., Karamitros, M., Kyriakou, I., Maigne, L., Meylan, S., Murakami, K., Okada, S., Payno, H., Perrot, Y., Petrovic, I., Pham, Q.T., Ristic-Fira, A., Sasaki, T., Štěpán, V., Tran, H.N., Villagrasa, C., Incerti, S., 2015. Track structure modeling in liquid water: A review of the geant4-dna very low energy extension of the geant4 monte carlo simulation toolkit. *Physica Medica: European Journal of Medical Physics* 31, 861–874. URL: <https://doi.org/10.1016/j.ejmp.2015.10.087>, doi:10.1016/j.ejmp.2015.10.087.

Casiraghi, M., Bashkirov, V., Hurley, F., Schulte, R., 2014. A novel approach to study radiation track structure with nanometer-equivalent resolution. *The European Physical Journal D* 68, 111. URL: <https://doi.org/10.1140/epjd/e2014-40841-0>, doi:10.1140/epjd/e2014-40841-0.

Casiraghi, M., Bashkirov, V.A., Hurley, R.F., Schulte, R.W., 2015. Characterisation of a track structure imaging detector. *Radiation Protection Dosimetry* 166, 223–227. URL: <https://doi.org/10.1093/rpd/ncv139>, doi:10.1093/rpd/ncv139, arXiv:<https://academic.oup.com/rpd/article-pdf/166/1-4/223/4565335/ncv139.pdf>.

Conte, V., Bianchi, A., Selva, A., 2023. Track structure of light ions: The link to radiobiology. *International Journal of Molecular Sciences* 24. URL: <https://www.mdpi.com/1422-0067/24/6/5826>, doi:10.3390/ijms24065826.

Conte, V., Selva, A., Colautti, P., Hilgers, G., Rabus, H., Bantsar, A., Pietrzak, M., Pszona, S., 2017. NANODOSIMETRY: TOWARDS A NEW CONCEPT OF RADIATION QUALITY. *Radiation Protection Dosimetry* 180, 150–156. URL: <https://doi.org/10.1093/rpd/ncx175>, doi:10.1093/rpd/ncx175, arXiv:<https://academic.oup.com/rpd/article-pdf/180/1-4/150/25409814/ncx175.pdf>.

van Elsbergen, V., Bachmann, P.K., Juestel, T., 2000. 16.3: Ion-induced secondary electron emission: A comparative study. *SID Symposium Digest of Technical Papers* 31, 220–223. URL: <https://sid.onlinelibrary.wiley.com/doi/abs/10.1889/1.1832922>, doi:<https://doi.org/10.1889/1.1832922>, arXiv:<https://sid.onlinelibrary.wiley.com/doi/pdf/10.1889/1.1832922>.

Faddegon, B., Blakely, E.A., Burigo, L., Censor, Y., Dokic, I., Kondo, N.D., Ortiz, R., Méndez, J.R., Rucinski, A., Schubert, K., Wahl, N., Schulte, R., 2023. Ionization detail parameters and cluster dose: a mathematical model for selection of nanodosimetric quantities for use in treatment planning in charged particle radiotherapy. *Physics in Medicine & Biology* 68, 175013. URL: <https://dx.doi.org/10.1088/1361-6560/acea16>, doi:10.1088/1361-6560/acea16.

Garty, G., Shchemelinin, S., Breskin, A., Chechik, R., Assaf, G., Orion, I., Bashkirov, V., Schulte, R., Grosswendt, B., 2002. The performance of a novel ion-counting nanodosimeter. *Nuclear Instruments and Methods in Physics Research Section A: Accelerators, Spectrometers, Detectors and Associated Equipment* 492, 212–235. URL: <https://www.sciencedirect.com/science/article/pii/S0168900202012780>, doi:[https://doi.org/10.1016/S0168-9002\(02\)01278-0](https://doi.org/10.1016/S0168-9002(02)01278-0).

Grosswendt, B., 2004. Recent advances of nanodosimetry. *Radiation Protection Dosimetry* 110, 789–799. URL: <https://doi.org/10.1093/rpd/nch171>, doi:10.1093/rpd/nch171, arXiv:<https://academic.oup.com/rpd/article-pdf/110/1-4/789/4529014/nch171.pdf>.

Grosswendt, B., De Nardo, L., Colautti, P., Pszona, S., Conte, V., Tornielli, G., 2004. Experimental equivalent cluster-size distributions in nanometric volumes of liquid water. *Radiation Protection Dosimetry* 110, 851–857. URL: <https://doi.org/10.1093/rpd/nch203>, doi:10.1093/rpd/nch203, arXiv:<https://academic.oup.com/rpd/article-pdf/110/1-4/851/4529938/nch203.pdf>.

Hilgers, G., Braunroth, T., Rabus, H., 2022. Characterisation of the ptb ion counter nanodosimeter's target volume and its equivalent size in terms of liquid h₂o. *Radiation Physics and Chemistry* 191, 109862. URL: <https://www.sciencedirect.com/science/article/pii/S0963174822000507>.

sciencedirect.com/science/article/pii/S0969806X21005120, doi:<https://doi.org/10.1016/j.radphyschem.2021.109862>.

Hilgers, G., Bug, M.U., Gargioni, E., Rabus, H., 2015. Secondary ionisations in a wall-less ion-counting nanodosimeter: quantitative analysis and the effect on the comparison of measured and simulated track structure parameters in nanometric volumes. *The European Physical Journal D* 69. URL: <https://doi.org/10.1140/epjd/e2015-60176-6>, doi:10.1140/epjd/e2015-60176-6.

Hilgers, G., Rabus, H., 2019. Reducing the background of secondary ions in an ion-counting nanodosimeter. *Journal of Instrumentation* 14, P07012. URL: <https://dx.doi.org/10.1088/1748-0221/14/07/P07012>, doi:10.1088/1748-0221/14/07/P07012.

Incerti, S., Baldacchino, G., Bernal, M., Capra, R., Champion, C., Francis, Z., Guèye, P., Mantero, A., Mascialino, B., Moretto, P., Nieminen, P., Villagrassa, C., Zacharatou, C., 2010a. The geant4-dna project. *International Journal of Modeling, Simulation, and Scientific Computing* 01, 157–178. URL: <https://doi.org/10.1142/S1793962310000122>, doi:10.1142/S1793962310000122, arXiv:<https://doi.org/10.1142/S1793962310000122>.

Incerti, S., Ivanchenko, A., Karamitros, M., Mantero, A., Moretto, P., Tran, H.N., Mascialino, B., Champion, C., Ivanchenko, V.N., Bernal, M.A., Francis, Z., Villagrassa, C., Baldacchino, G., Guèye, P., Capra, R., Nieminen, P., Zacharatou, C., 2010b. Comparison of geant4 very low energy cross section models with experimental data in water. *Medical Physics* 37, 4692–4708. URL: <https://aapm.onlinelibrary.wiley.com/doi/abs/10.1118/1.3476457>, doi:<https://doi.org/10.1118/1.3476457>, arXiv:<https://aapm.onlinelibrary.wiley.com/doi/pdf/10.1118/1.3476457>.

Incerti, S., Kyriakou, I., Bernal, M.A., Bordage, M.C., Francis, Z., Guatelli, S., Ivanchenko, V., Karamitros, M., Lampe, N., Lee, S.B., Meylan, S., Min, C.H., Shin, W.G., Nieminen, P., Sakata, D., Tang, N., Villagrassa, C., Tran, H.N., Brown, J.M.C., 2018. Geant4-dna example applications for track structure simulations in liquid water: A report from the geant4-dna project. *Medical Physics* 45, e722–e739. URL: <https://aapm.onlinelibrary.wiley.com/doi/abs/10.1002/mp.13048>, doi:<https://doi.org/10.1002/mp.13048>, arXiv:<https://aapm.onlinelibrary.wiley.com/doi/pdf/10.1002/mp.13048>.

JCGM, 2023. Guide to the expression of uncertainty in measurement. Bureau International des Poids et Mesures (BIPM). URL: https://www.bipm.org/documents/20126/194484570/JCGM_GUM-1/74e7aa56-2403-7037-f975-cd6b555b80e6.

Kempf, I., Hoffmann, T.M., Besserer, J., Schneider, U., 2025. Development and characterization of a compact nanodosimetric detector. *Nuclear Instruments and Methods in Physics Research Section A: Accelerators, Spectrometers, Detectors and Associated Equipment* 1075, 170337. URL: <https://www.>

[sciencedirect.com/science/article/pii/S016890022500138X](https://www.sciencedirect.com/science/article/pii/S016890022500138X), doi:<https://doi.org/10.1016/j.nima.2025.170337>.

Kempf, I., Schneider, U., 2024. Monte carlo model for ion mobility and diffusion for characteristic electric fields in nanodosimetry. *Zeitschrift für Medizinische Physik* 34, 140–152. URL: <https://www.sciencedirect.com/science/article/pii/S0939388922001398>, doi:<https://doi.org/10.1016/j.zemedi.2022.12.006>. special Issue: Space Radiation Research.

Kempf, I., Schneider, U., 2025. Diffusion and mobility measurements for propane gas with a nanodosimetric detector. *Radiation Physics and Chemistry* 226, 112274. URL: <https://www.sciencedirect.com/science/article/pii/S0969806X24007667>, doi:<https://doi.org/10.1016/j.radphyschem.2024.112274>.

Kim, D.I., Lim, Y.G., Kim, Y.G., Ko, J.J., Lee, C.W., Cho, G.S., Choi, E.H., 2000. Ion-induced secondary electron emission coefficient (γ) of bulk mgo-single crystals. *Jpn. J. Appl. Phys.* 39, 1890–1891. URL: <https://iopscience.iop.org/article/10.1143/JJAP.39.1890/pdf>.

Malinen, M., Råback, P., 2013. Elmer finite element solver for multiphysics and multiscale problems. In book: *Multiscale Modelling Methods for Applications in Material Science*.

Merza, V., Bancer, A., Belchior, A., Brzozowska, B., Canhoto, J.F., Katmeh, K., Pietrzak, M., Ruciński, A., Schulte, R., 2025. Garfield++ and geant4-dna simulation of a compact thgem-based nanodosimeter. *Nuclear Instruments and Methods in Physics Research Section A: Accelerators, Spectrometers, Detectors and Associated Equipment* 1080, 170729. URL: <https://www.sciencedirect.com/science/article/pii/S0168900225005303>, doi:<https://doi.org/10.1016/j.nima.2025.170729>.

Nardo, L.D., Colautti, P., Conte, V., Baek, W., Grosswendt, B., Tornielli, G., 2002. Ionization-cluster distributions of α -particles in nanometric volumes of propane: measurement and calculation. *Radiation and Environmental Biophysics* 41, 235–256. URL: <https://doi.org/10.1007/s00411-002-0171-6>, doi:[10.1007/s00411-002-0171-6](https://doi.org/10.1007/s00411-002-0171-6).

Pietrzak, M., Pszona, S., Bantsar, A., 2018. Measurements of spatial correlations of ionisation clusters in the track of carbon ions-first results. *Radiation Protection Dosimetry* 180, 162–167. URL: <https://doi.org/10.1093/rpd/ncy079>, doi:[10.1093/rpd/ncy079](https://doi.org/10.1093/rpd/ncy079).

Pszona, S., Kula, J., Marjanska, S., 2000. A new method for measuring ion clusters produced by charged particles in nanometre track sections of dna size. *Nuclear Instruments and Methods in Physics Research Section A: Accelerators, Spectrometers, Detectors and Associated Equipment* 447, 601–607. URL: <https://www.sciencedirect.com/science/article/pii/S0168900299011912>, doi:[https://doi.org/10.1016/S0168-9002\(99\)01191-2](https://doi.org/10.1016/S0168-9002(99)01191-2).

Rucinski, A., Biernacka, A., Schulte, R., 2021. Applications of nanodosimetry in particle therapy planning and beyond. *Physics in Medicine & Biology* 66, 24TR01. URL: <https://dx.doi.org/10.1088/1361-6560/ac35f1>, doi:10.1088/1361-6560/ac35f1.

Schindler, H., 2025. Garfield++ User Guide Version 2025.1. URL: <https://garfieldpp.web.cern.ch/garfieldpp/>.

Tran, H.N., Archer, J., Baldacchino, G., Brown, J.M.C., Chappuis, F., Cirrone, G.A.P., Desorgher, L., Dominguez, N., Fattori, S., Guatelli, S., Ivantchenko, V., Méndez, J.R., Nieminen, P., Perrot, Y., Sakata, D., Santin, G., Shin, W.G., Villagrasa, C., Zein, S., Incerti, S., 2024. Review of chemical models and applications in geant4-dna: Report from the esa biorad iii project. *Medical Physics* 51, 5873–5889. URL: <https://aapm.onlinelibrary.wiley.com/doi/abs/10.1002/mp.17256>, doi:<https://doi.org/10.1002/mp.17256>, arXiv:<https://aapm.onlinelibrary.wiley.com/doi/pdf/10.1002/mp.17256>.

Vance, D.W., 1968a. Auger electron emission from clean mo bombarded by positive ions. ii. effect of angle of incidence. *Phys. Rev.* 169, 252–262. URL: <https://link.aps.org/doi/10.1103/PhysRev.169.252>, doi:10.1103/PhysRev.169.252.

Vance, D.W., 1968b. Auger electron emission from clean mo bombarded by positive ions. iii. effect of electronically excited ions. *Phys. Rev.* 169, 263–272. URL: <https://link.aps.org/doi/10.1103/PhysRev.169.263>, doi:10.1103/PhysRev.169.263.

Vasi, F., Kempf, I., Besserer, J., Schneider, U., 2021. Fire: A compact nanodosimeter detector based on ion amplification in gas. *Nuclear Instruments and Methods in Physics Research Section A: Accelerators, Spectrometers, Detectors and Associated Equipment* 999, 165116. URL: <https://www.sciencedirect.com/science/article/pii/S0168900221001005>, doi:<https://doi.org/10.1016/j.nima.2021.165116>.

Wang, J., Wang, Y., Zhu, X., Ding, W., Li, Y., Cheng, J., Herrmann, N., Deppner, I., Zhang, Y., Loizeau, P., Senger, P., Gonzalez-Diaz, D., 2010. Development of multi-gap resistive plate chambers with low-resistive silicate glass electrodes for operation at high particle fluxes and large transported charges. *Nuclear Instruments and Methods in Physics Research Section A: Accelerators, Spectrometers, Detectors and Associated Equipment* 621, 151–156. URL: <https://www.sciencedirect.com/science/article/pii/S0168900210009058>, doi:<https://doi.org/10.1016/j.nima.2010.04.056>.

Wang, Y., Zhang, Q., Han, D., Wang, F., Yu, Y., Lyu, P., Li, Y., 2019. Status of technology of mrpc time of flight system. *Journal of Instrumentation* 14, C06015. URL: <https://doi.org/10.1088/1748-0221/14/06/C06015>, doi:10.1088/1748-0221/14/06/C06015.